Experimental and theoretical studies of the electronic transport of an extended curcuminoid in graphene nano-junctions

Teresa Cardona-Lamarca,[a¥] Thomas Y. Baum,[b¥] Rossella Zaffino,*[a] Daniel Herrera,[a] Raphael Pfattner,[a] Silvia Gómez-Coca,[c,d] Eliseo Ruiz,*[c,d] Arántzazu González-Campo,*[a] Herre S. J. van der Zant *[b] and Núria Aliaga-Alcalde*[a,e]

[a] *ICMAB-CSIC (Institut de Ciència de Materials de Barcelona), Campus de la Universitat Autònoma de Barcelona, 08193, Bellaterra, Spain*

[b] *Kavli Insititute of Nanoscience, Delft University of Technology, Lorentzweg 1, Delft 2628 CJ, The Netherlands.*

[c] *Departament de Química Inorgànica i ORgànica and Institut de Nanociéncia i Nanotecnología, Universitat de Barcelona, Diagonal 645, 08028, Barcelona, Spain.*

[d] *Departament de Química Inorgànica i Orgànica and Institute de Recerca de Química Teòrica i Computacional, Universitat de Barcelona, Diagonal 645, E-08028, Barcelona, Spain.*

[e] *ICREA (Institució Catalana de Recerca i Estudis Avançats), Passeig Lluís Companys 23, 08018, Barcelona, Spain.*

[¥] These authors contributed equally

Contents:

1. Materials for chemical synthesis.

Acetylacetonate ($C_5H_7O_2$, acac), boron trioxide (B_2O_3), tributyl borate ($(BuO)_3B$, $C_{12}H_{27}BO_3$), n-butyl amine (n-$BuNH_2$, $C_4H_{11}N$), 4- aminobenzyl alcohol ($H_2NC_6H_4CH_2OH$), potassium permanganate ($KMnO_4$), manganese (II) sulfate monohydrate ($MnSO_4{\cdot}H_2O$), sodium hydroxide (NaOH), 1- pyrenecarboxaldehyde, thionyl chloride ($SOCl_2$) and triethylamine (Et_3N) were provided by Sigma Aldrich, ABCR, Fluorochem and TCI Chemicals. Dimethylformamide (DMF), Diethyl ether (Et_2O), dichloromethane (DCM), acetone, tetrahydrofurane (THF), acetonitrile (ACN), 1,1,2,2-tetrachloroethane (TCE) and chloroform ($CHCl_3$) were purchased at Carlo Erba and Scharlab.

2. Measurements

^{1}H-NMR and ^{13}C-NMR spectra were recorded on a Bruker Avance III spectometer at 298 K at Servei RMN from Universitat Autonoma de Barcelona (UAB). Fourier transform infrared (FTIR) spectra were measured on a JASCO 4700LE FT-IR between 400 and 4000 cm^{-1}. UV/Vis absorption spectra were obtained with a JASCO V-780 UV/Vis/NIR spectrophotometer using quartz cells in a 200–800 nm range in transmittance mode. Elemental analysises were performed with a Thermo Scientific Flash 2000 and Flash Smart elemental analyser. MALDI-TOF mass spectra were obtained with a Bruker ULTRAFLEXTREME mass spectrometer at Servei de Proteòmica I Biologia Estructural from UAB and Servei de Proteómica i imatge from Institut de Quimica Avanzada de Catalunya (IQAC). Electrochemical measurements were conducted in a three electrodes cell using reference and auxiliary platinum electrodes and glassy carbon working electrode with a 0.1 M solution of tetrabutylammonium hexafluorophosphate ($TBAPF_6$) in THF as electrolyte. The experiments were registered at 50 mV/s in a Biologic SP-50 potentiostat and referenced versus ferrocene/ferrocenium couple, used as an internal reference. Fluorescence experiments were performed using a Fluorimeter NanologTM Horib Jobin Yvon IHR320 (detects fluorescence in the near-IR from 800 to 1700 nm). An integrating sphere was used to measure the quantum yields of **1** and **2**.

3. Synthetic procedures

3.1 Synthesis of MnO_2[1]

An aqueous solution of $MnSO_4$ (11.5 g, 68.0 mmol in 20 mL Milli-Q water) and NaOH (14 g, 350 mmol in 16.5 mL Milli-Q water) was added dropwise to a solution of $KMnO_4$ (13.0 g, 85.2 mmol in 80 mL Milli-Q water) heated at 40 °C. After 1 h, the reaction was cooled to room temperature, filtered through a filter plate and thoroughly washed with Milli-Q water. Finally, the product was dried in an oven at 100 °C for 3 nights. Yield 60 %

3.2 Synthesis of 4-aminobenzaldehyde[2]

9 g of freshly synthesized MnO_2 (103.5 mmol) was added into a solution of 4-aminobenzyl alcohol (2.00 g, 16.2 mmol) in 48 mL of dry DCM. After 2 days, the mixture was filtered through celite and the solvent was evaporated under vacuum to provide 4-aminobenzaldehyde in 94 % yield. ^{1}H-NMR (360 MHz, $CDCl_3$) δ: 9.73 (1H, s) 7.69 (2H, d, J=8.5 Hz), 6.69 (2H, d, J=8.5 Hz) 4.35

(2H, s). ^{13}C NMR (90 MHz, $CDCl_3$) δ: 190.6, 152.7, 132.4, 127.5, 114.2. MS MALDI-TOF (m/z) calculated for 4-aminobenzaldehyde: 121.0 [M]; found: 122.0 [M+1].

3.2 Synthesis of 1-pyrenecarboxylic acid (pyCOOH)[3]

A solution of $KMnO_4$ (664 mg, 4.2 mmol) in 50 mL of Milli-Q water was refluxed with a solution of 1- pyrenecarboxaldehyde (250 mg, 0.108 mmol) in 50 mL acetone for 24 h. Subsequently, the mixture was filtered and extracted with DCM. Afterwards, the aqueous phase was acidified until reaching pH=2 and centrifuged to isolate the product in 59% Yield. ^{1}H-NMR (400 MHz, DMSO-d6) δ: 13.30 (b, 1H) 9.24 (1H, d, J=9.4 Hz), 8.62 (1H, d, J=8.1 Hz) 8.43 (5H, m), 8.27 (1H, d, J= 8.7 Hz), 8.18 (1H, t, J=7.8 Hz). MS MALDI - TOF (m/z): calculated for PyCOOH: 246.07 [M]; found: 245.10 [M-1].

3.3 Synthesis of NH_2CCMoid (1)

78 µL of acetylacetone (0.77 mmol) and 53.7 mg of B_2O_3 (0.77 mmol) in 0.5 mL of DMF were heated at 80 °C for 30 minutes. Then sequentially, at an interval of 30 min., 0.83 mL of tributylborate (3.07 mmol) and a solution of 425 mg of 4-aminobenzaldehyde (3.50 mmol) in 1 mL of DMF were added. The mixture was allowed to evolve at 80 °C for half an hour before the dropwise addition of a solution of 30 µL of butylamine (0.30 mmol) in 0.4 mL DMF. The reaction was kept at 80 °C for a total of 4 hours and subsequently 6 mL of Milli-Q water were added allowing the mixture to cool to RT while stirring for 1 extra hour. Finally, the reaction was filtered, washed with Milli-Q water and dried with Et_2O. Yield 30 %. ^{1}H NMR (360 MHz, $CDCl_3$) δ: 16.20 (1H, s) 7.59 (2H, d, J=15.9 Hz), 7.40 (4H, d, J=8.2 Hz) 6.67 (4H, d, J= 8.2 Hz), 6.45 (2H, d, J= 15.9 Hz), 5.73 (1H, s), 3.94 (4 H, s). ^{13}C NMR (90 MHz, $CDCl_3$) δ:183.6, 148.7, 140.7, 130.1, 125.7, 120.3, 115.1. Elemental analysis calculated for $C_{19}H_{18}N_2O_2 \cdot 0.5\ H_2O$: C: 72.36 %; H: 6.07 %; N: 8.88 %; O: 12.68 %, found: C 72.20 %; H 5.66 %; N: 9.00 %; O: 13.14 %; MS MALDI - TOF (m/z) calculated for NH_2CCMoid: 306.1 [M]; found: 304.9 [M-1].

3.4 Synthesis of hemi-NH_2CCMoid

Hemi-NH_2CCMoid was obtained as a byproduct in the previous reaction in an 8 % yield. The mother liquid from the final filtration described for **2** contained Hemi-NH_2CCMoid as a thin precipitate. It was then isolated by centrifugation, washed with Milli-Q water and dried with Et_2O. ^{1}H NMR (360 MHz, $CDCl_3$) δ: 15.58 (1H, s) 7.55 (1H, d, J=15.9 Hz), 7.37 (2H, d, J=8.4 Hz) 6.67 (2H, d, J= 8.4 Hz), 6.30 (1H, d, J= 15.9 Hz), 5.59 (1H, s), 3.94 (2H, s), 2.14 (3H, s). ^{13}C NMR (100 MHz, $CDCl_3$) δ: 196.3, 140.6, 130.0, 118.7, 115.1, 110.13, 100.5, 26.8. Elemental analysis calculated for $C_{12}H_{13}NO_2 \cdot 0.5\ H_2O$: C 67.94 %; H: 6.65 %; N: 6.60 %; O: 18.31 %, found: C 67.98 %; H: 6.33%; N: 7.23 %; O: 18.46 %; MS MALDI- TOF (m/z) calculated for Hemi-NH_2CCMoid: 203.1 [M]; found: 202.1 [M-1].

13.5 Synthesis of pyACCMoid (2)

30 mg pyCOOH (0.12 mmol) were dissolved in 0.8 mL of $SOCl_2$ (11.2 mmol) and refluxed for 3 hours. Subsequently, the excess of $SOCl_2$ was removed under vacuum. A solution of the product in 5 mL of dry THF was transferred into a microwave (MW) vial, together with 16 µL of Et_3N (0.11 mmol), and a dispersion of NH_2CCMoid (18.4 mg, 0.06 mmol) in 12 mL of dry THF. The mixture was placed into the MW reactor at 60°C for 90 minutes. After that time, the mixture was filtered off, the solvent evaporated, and the product was washed with hot ACN to obtain **2** as a solid in a 25 % yield. ^{1}H NMR (400 MHz, DMSO-d6) δ: 16.28 (1H, s), 10.98 (2H, s), 8.51 (2H, d, J=9.1 Hz), 8.43 (16H, m) 8.33 (9H, m), 8.17 (2H, t, J= 7.4 Hz), 7.99 (4H, d, J= 8.8 Hz), 7.82 (2H, d, J= 8.8 Hz),

7.70 (2H, d, J= 16.1 Hz), 6.95 (2H, d, J= 16.1 Hz), 6.20 (1H, s); Elemental analysis calculated for $C_{53}H_{42}N_2O_4 \cdot 4\ H_2O$: C 76.24 %; H: 5.07 %; N: 3.36 % found: C: 76.86 %; H: 4.25 %; N: 3.35 %; MS MALDI - TOF (m/z): calculated for PyACCMoid: 762.2 [M]; found: 761.3 [M-1].

4. Molecular characterisation

4.1 NH_2CCMoid (1)

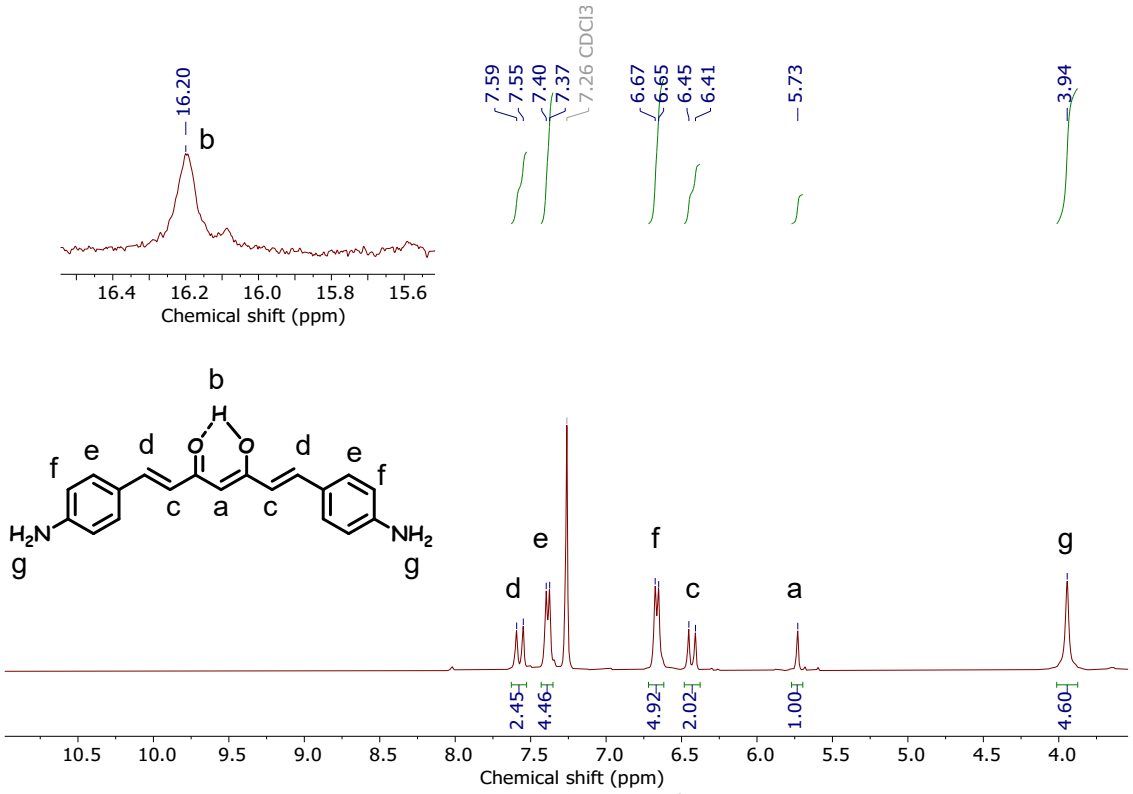

Figure S1. ^{1}H-NMR spectrum of **1** in $CDCl_3$.

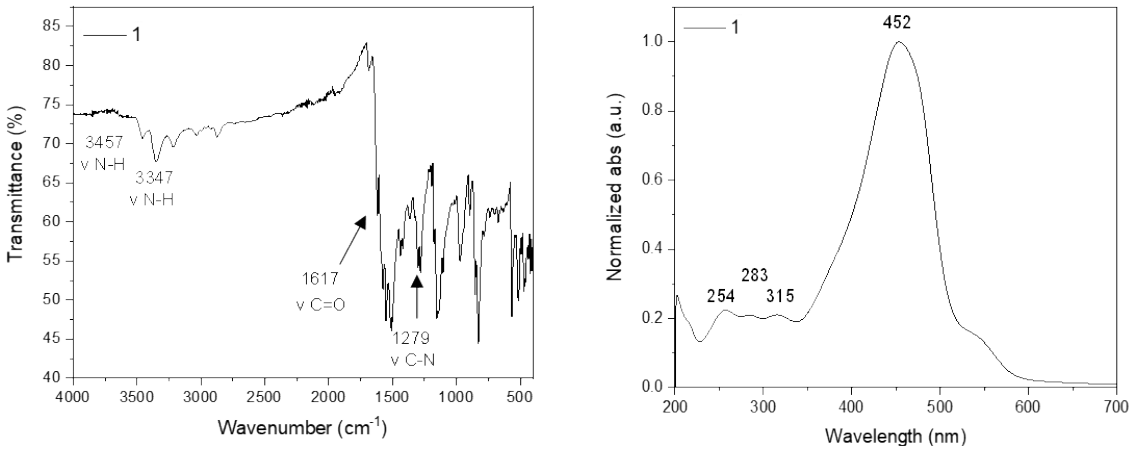

Figure S2. (Left) ATR-FTIR spectrum of **1**. (Right) UV-vis absorption spectrum of **1** in THF.

The solvochromic behaviour of CCMoids **1** hinders the estimation of the energy bandgap from the solution spectra. For this reason, we performed the estimation of the bandgap using absorption spectroscopy in the solid-state and Tauc's equation as described in Eq S1:

$$(\alpha h\nu)^{1/n} = A\ (h\nu - E_g) \qquad (Eq.\ S1)$$

Where:

$$\alpha(absorption\ coefficient) = \frac{2.303\ *\ absorbance}{l}$$

l = sample thickness (cm)

h =Plank's constant (J/s)

$$\nu = photon\ frequency = \frac{c}{wavelength\ (m)}$$

c = speed of light (m/s)

n=1/2 (for direct allowed transitions)

A= proportionality constant

Plotting the $(\alpha h\nu)^{1/n}$ versus $(h\nu)$, the optical bandgap, Eg_{op}, corresponds to the intersection between the *x* axis with the tangent of the curve.

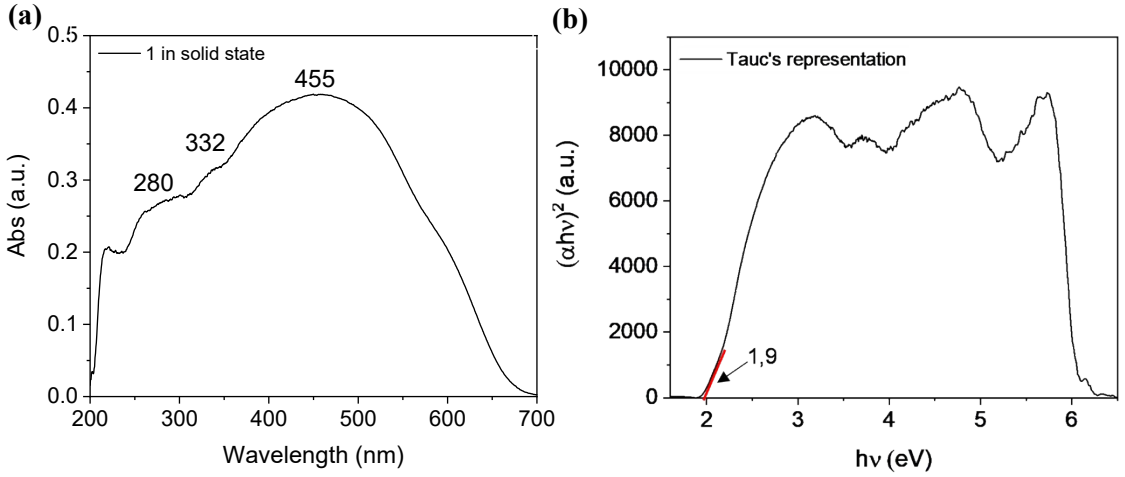

Figure S3. (a) Solid-state UV-vis absorption spectrum of **1 (b)** Tauc's representation of the solid-state spectrum of **1**.

The differential pulse voltammetry (DPV) plot was employed to estimate the HOMO-LUMO values, which can be related to the energy required to extract or to introduce an electron. Therefore, they can be correlated to the first electrochemical oxidation and reduction potentials, as indicated by Eqs. S2 and S3 below:

$$E_{HOMO} = -\left(E_{onset\ oxidation}\right) + 4.8 \qquad (Eq.\ S2)$$

$$E_{LUMO} = -\left(E_{onset\ reduction}\right) + 4.8 \qquad (Eq.\ S3)$$

Where 4.8 eV is the energy level value of the Fc/Fc^{+} pair in vacuum. Finally, the bandgap energy can be calculated following Eq S4:

$$E_g = (E_{HOMO}) - (E_{LUMO}) \qquad (Eq.\ S4)$$

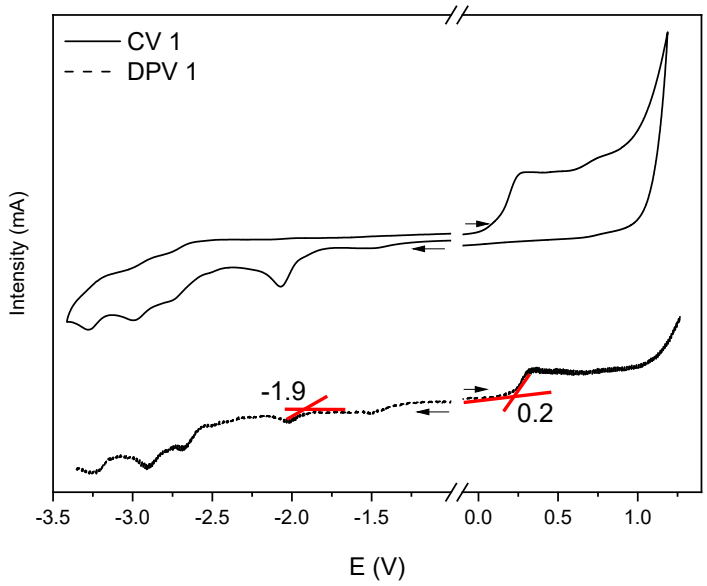

Figure S4. Cyclic voltammetry (CV) and differential pulse voltammetry (DPV) of **1**.

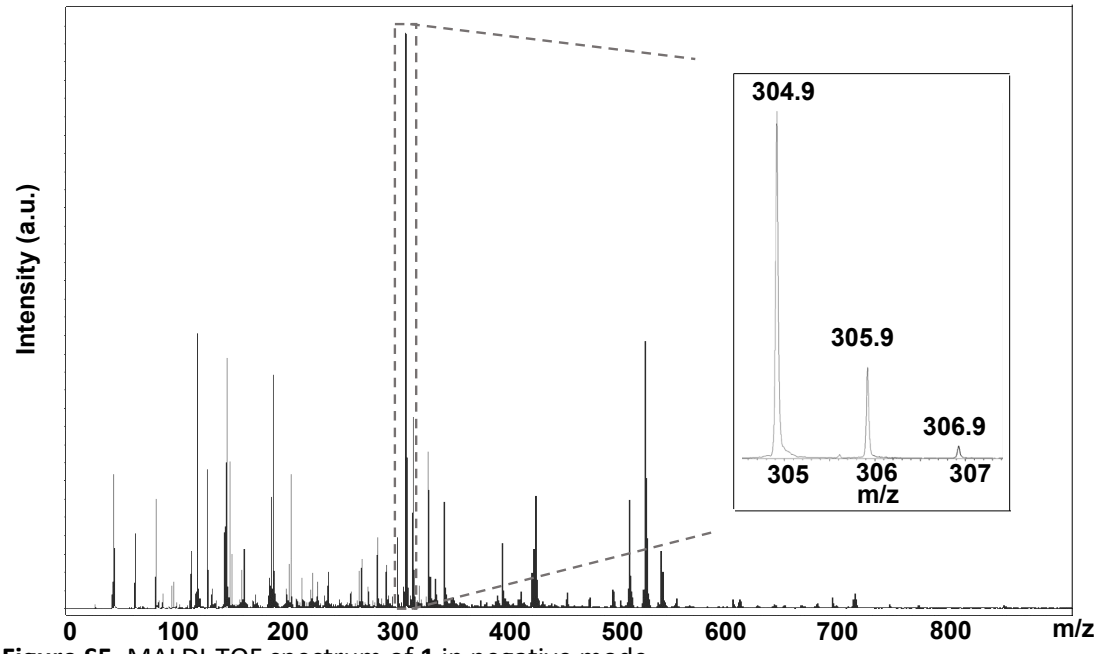

Figure S5. MALDI-TOF spectrum of **1** in negative mode.

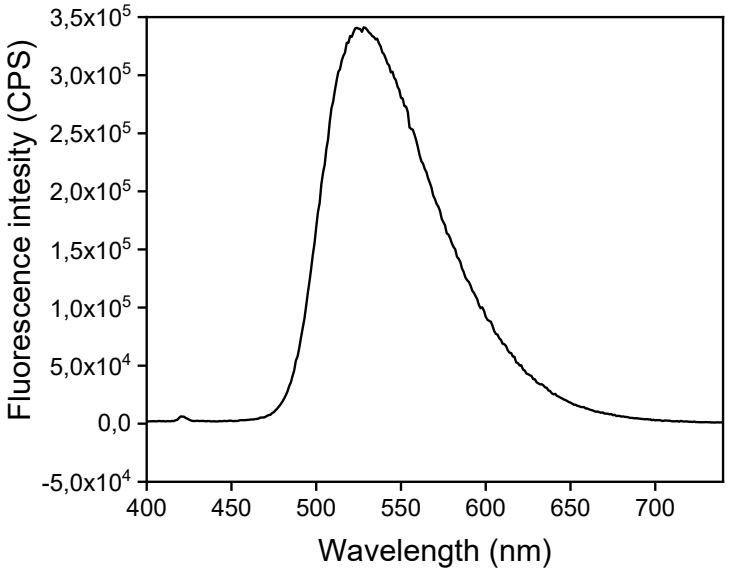

Figure S6. Fluorescence spectrum of **1** in THF at RT. The excitation wavelength (λ_{exc}) is 375 nm. QY= 1.48%

4.2 Hemi-NH_2CCMoid

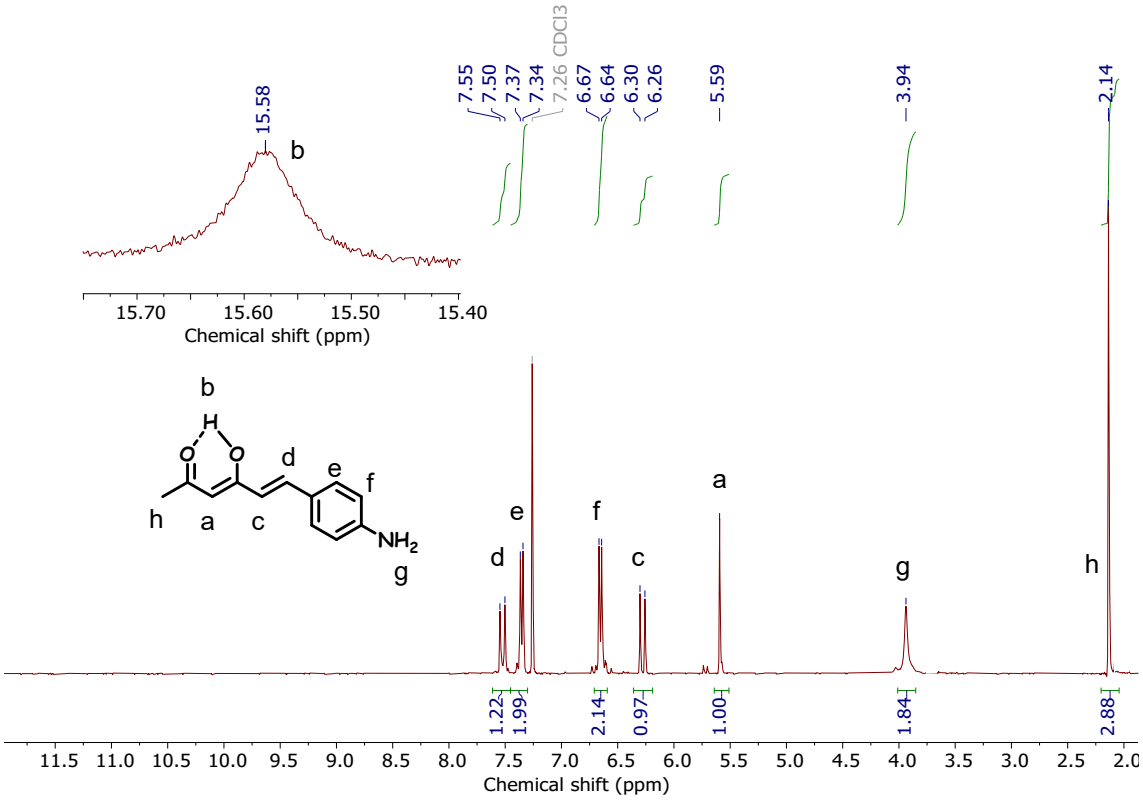

Figure S7. ^{1}H-NMR spectrum of Hemi-NH_2CCMoid in $CDCl_3$.

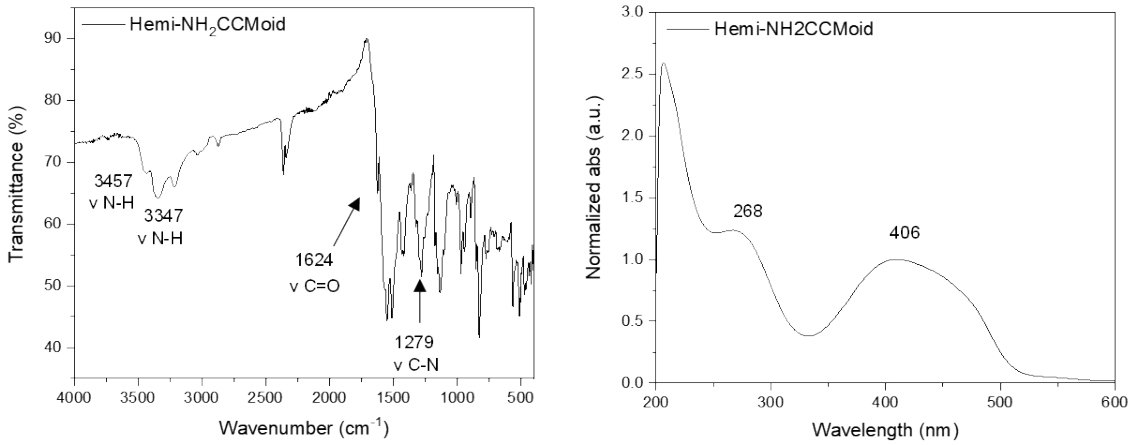

Figure S8. (Left) ATR-FTIR spectrum of Hemi-NH_2CCMoid. (Right) UV-Vis absorption spectrum of Hemi-NH_2CCMoid in THF.

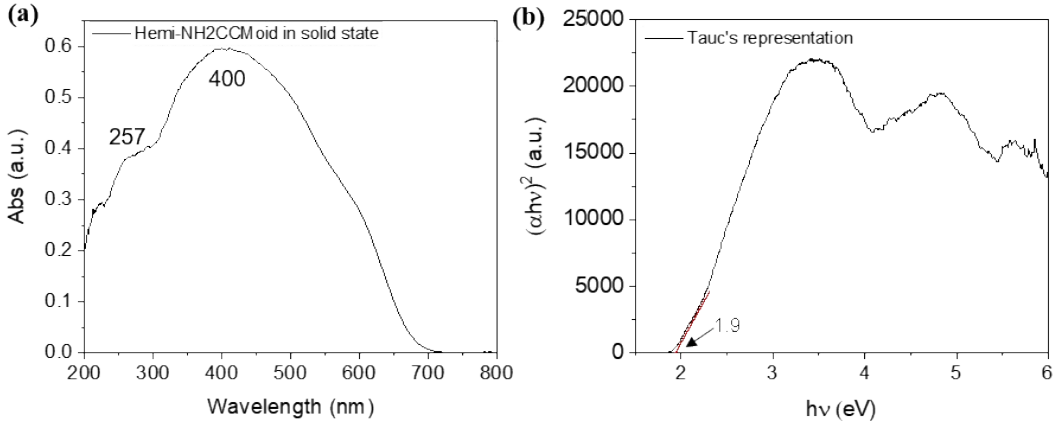

Figure S9. (a) Solid-state UV-vis absorption spectrum of hemi-NH_2CCMoid (b) Tauc's representation of the solid-state spectrum of Hemi- NH_2CCMoid.

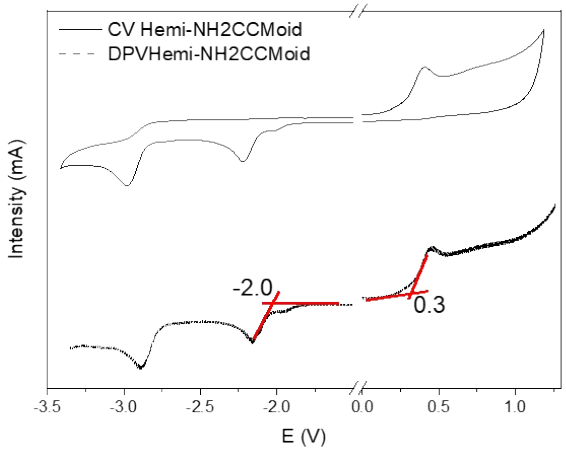

Figure S10. CV and DPV of the Hemi-NH_2CCMoid.

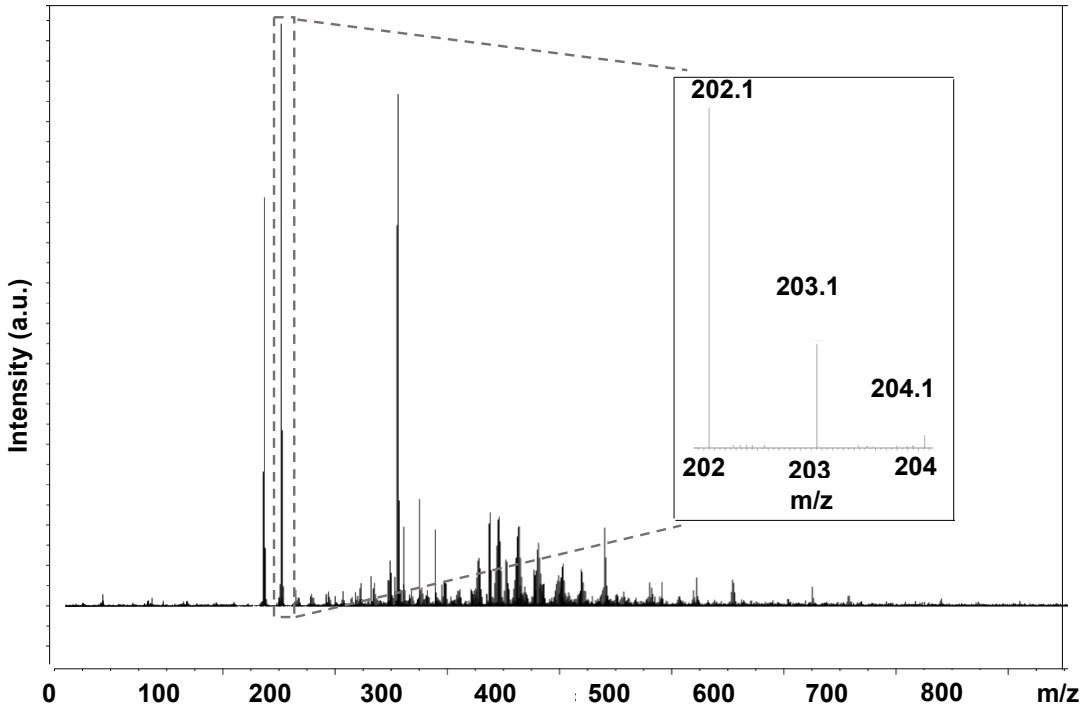

Figure S11. MALDI-TOF spectrum of Hemi-NH_2CCMoid in negative mode.

4.2 pyACCMoid (2)

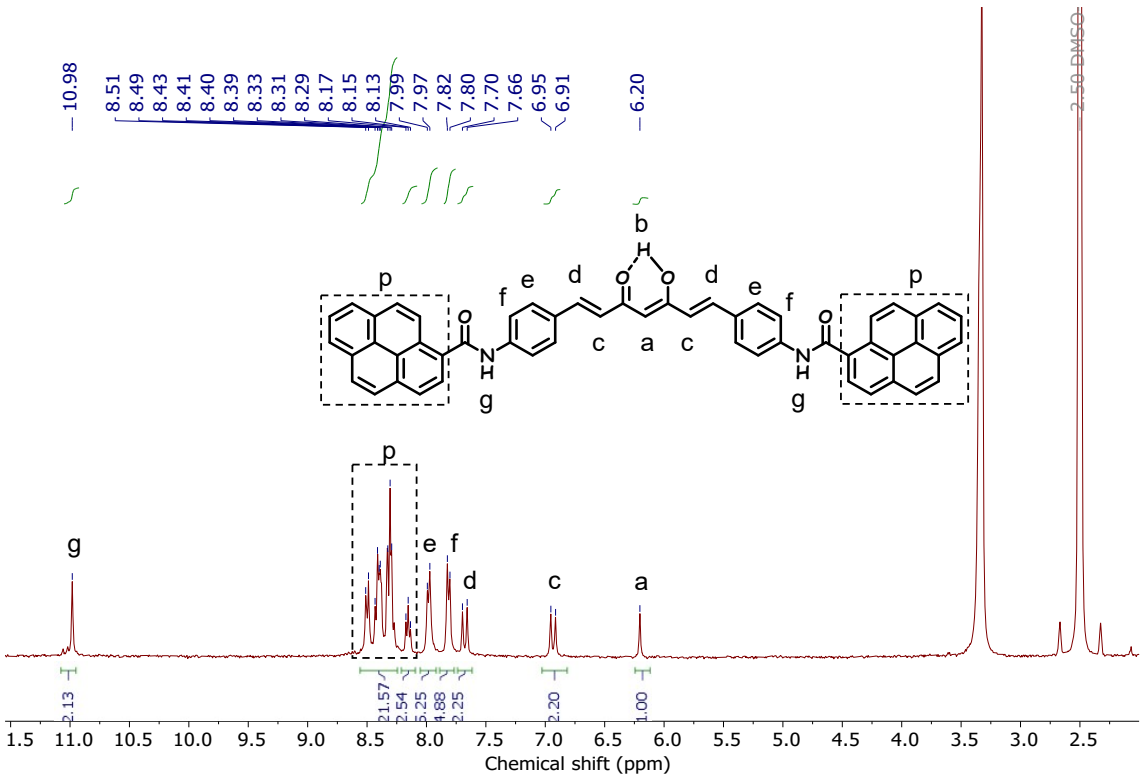

Figure S12. ^{1}H-NMR spectrum of **2** in DMSO-d_6.

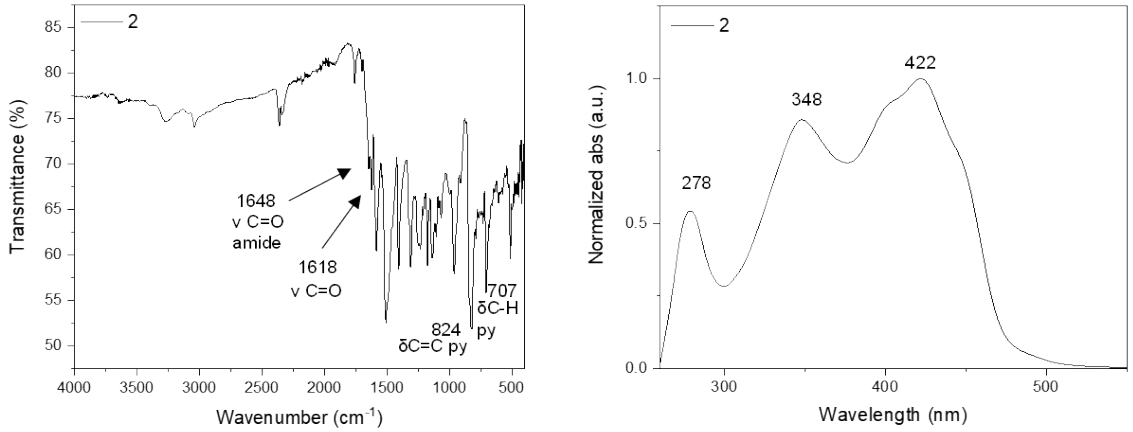

Figure S13. (Left) ATR-FTIR spectrum of **2**. (Right) UV-vis absorption spectrum of **2** in THF.

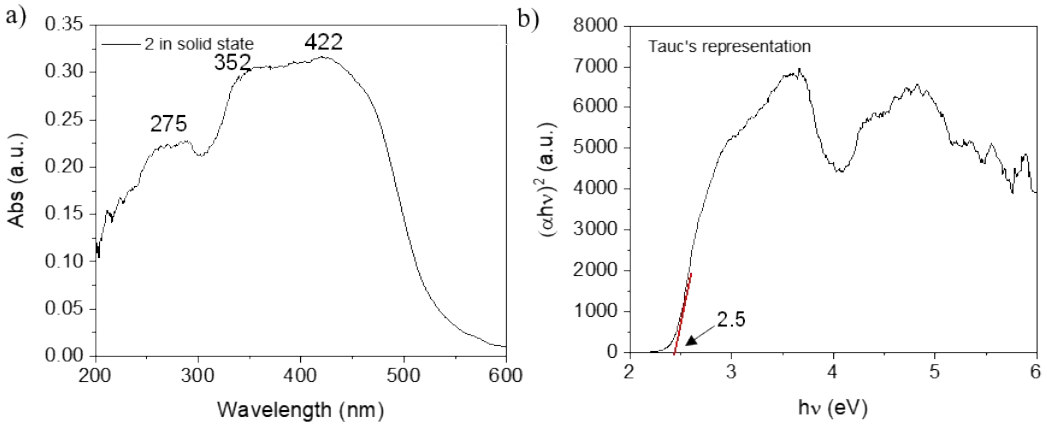

Figure S14. **(a)** Solid-state UV-vis absorption spectrum of **2 (b)** Tauc's representation of the solid-state spectrum of **2**.

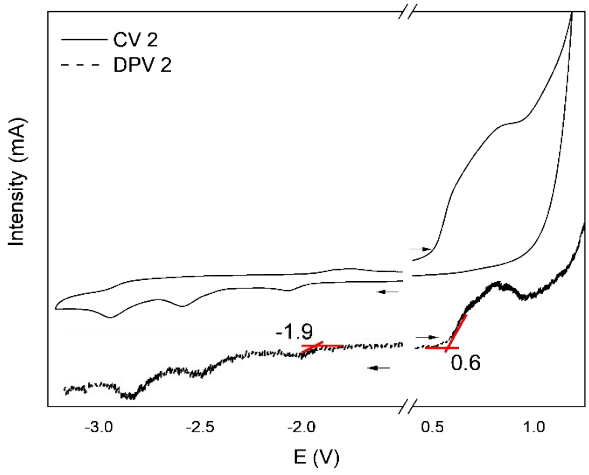

Figure S15. CV and DPV of **2**.

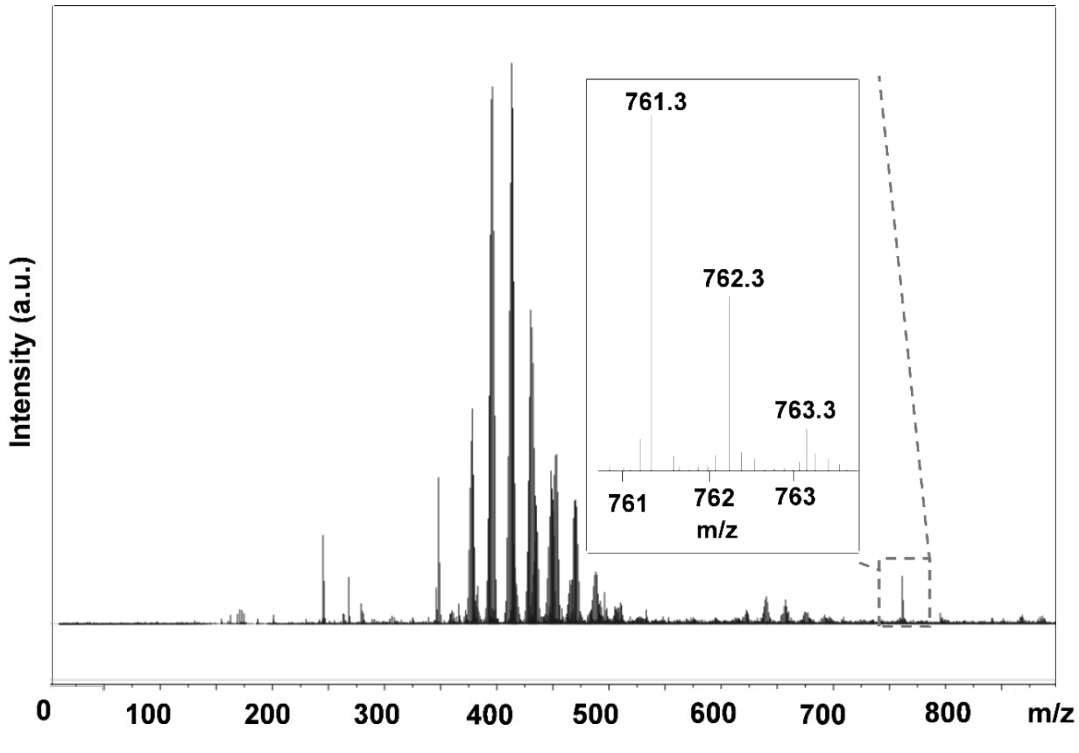

Figure S16. MALDI-TOF spectrum of **2** in negative mode.

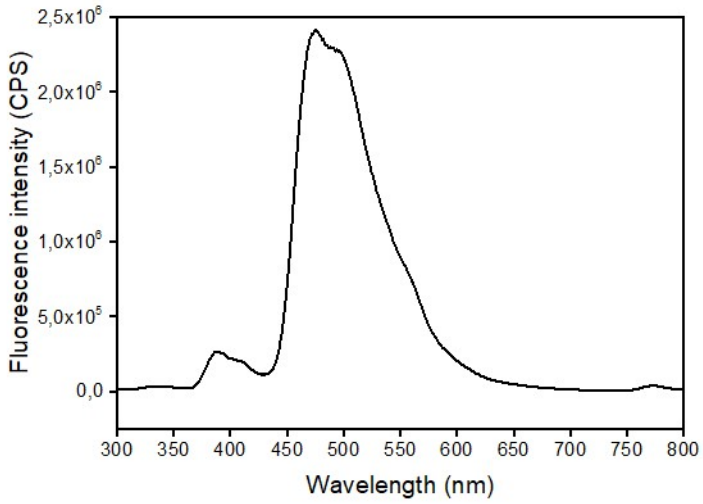

Figure S17. Fluorescence spectrum of compound **2** in THF at RT. The excitation wavelength (λ_{exc}) is 280 nm. QY= 0.84%.

4.4 Energetic diagram of CCMoid 1 and 2 estimated by electrochemistry

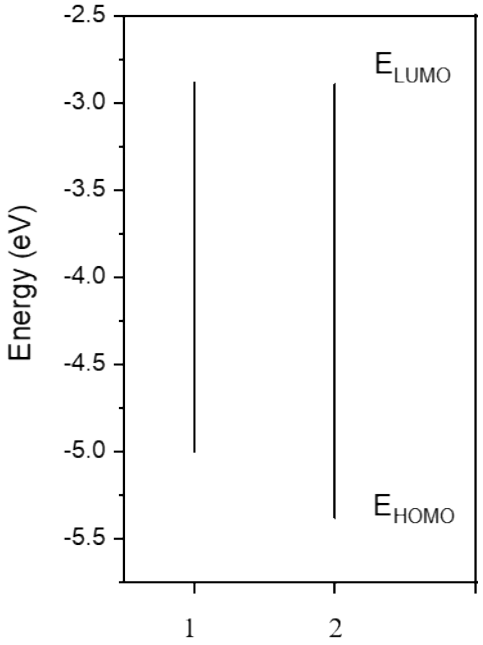

Figure S18. HOMO and LUMO energetic diagram of compounds **1** and **2**.

CCMoids	$Eg_{op(exp)}$	$Eg_{elec(exp)}$	$HOMO_{exp}$	$LUMO_{exp}$	B3LYP-TDDFT	B3LYP	HOMO-B3LYP	LUMO-B3LYP
1	2.0	2.1	-5.0	-2.9	2.7	3.2	-5.3	**-2.1**
2	**2.5**	**2.5**	**-5.4**	**-2.9**	**2.6(2.5)**	**3.0(2.9)**	**-5.8(-5.8)**	**-2.8(-2.9)**

Tab S1. List of experimental and theoretical energetic data (in eV) and comparison between systems **1**-**2**.

5. Theoretical calculations: part I.

Full consistent non-equilibrium Green function (NEGF) calculations[5,6] were performed using the ATK program (2022.12 version).[7] The PBE exchange-correlation functional[8] was used together with numerical wavefunction of double-z quality with polarization for all the atoms except the gold atoms using a single- z quality with polarization. A total number of 384 k-points was used to calculate the energy and wavefunction properties. Molecular calculations were performed with Gaussian09 code[9] using B3LYP functional[10] with a 6-311G* basis set, either ground state or time-dependent density functional calculations.

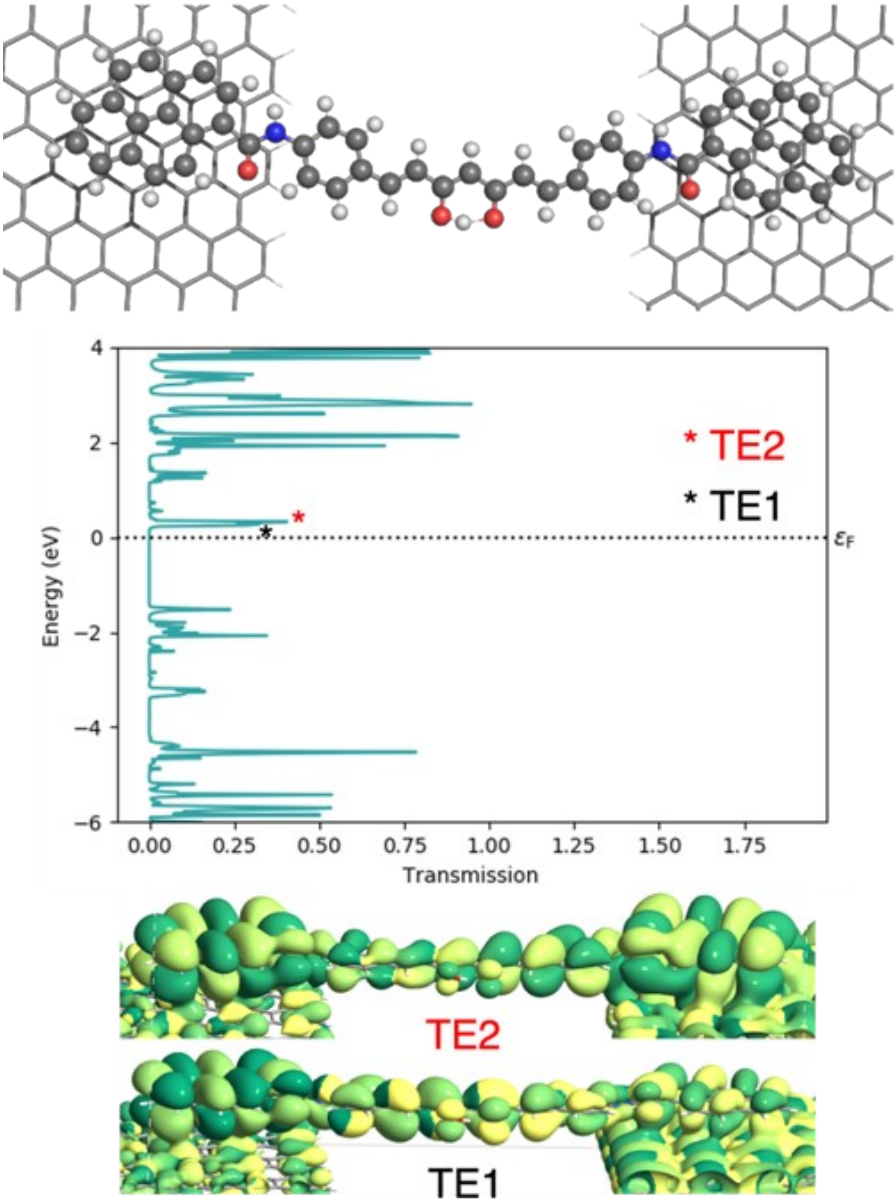

Figure S19. (a) DFT optimised structure of pyACCMoid on a given GNJ (corresponding to model **2A** in Figure 3a). (b) The transmission spectrum for the system shown above. (c) Transmission eigenfunctions corresponding to the first two empty peaks in the transmission spectrum are highlighted with an asterisk. Transmission eigenfunctions are plotted for some frontier orbitals. The transmission eigenfunctions are obtained by diagonalising the transmission matrix, and the

corresponding transmission eigenvalues indicate the importance of each eigenfunction in transport. As it is a complex wave function, the colour map represents the phase of the function from 0 to 2π from dark green to yellow colours. The threshold value employed for the isosurfaces is 0.1.

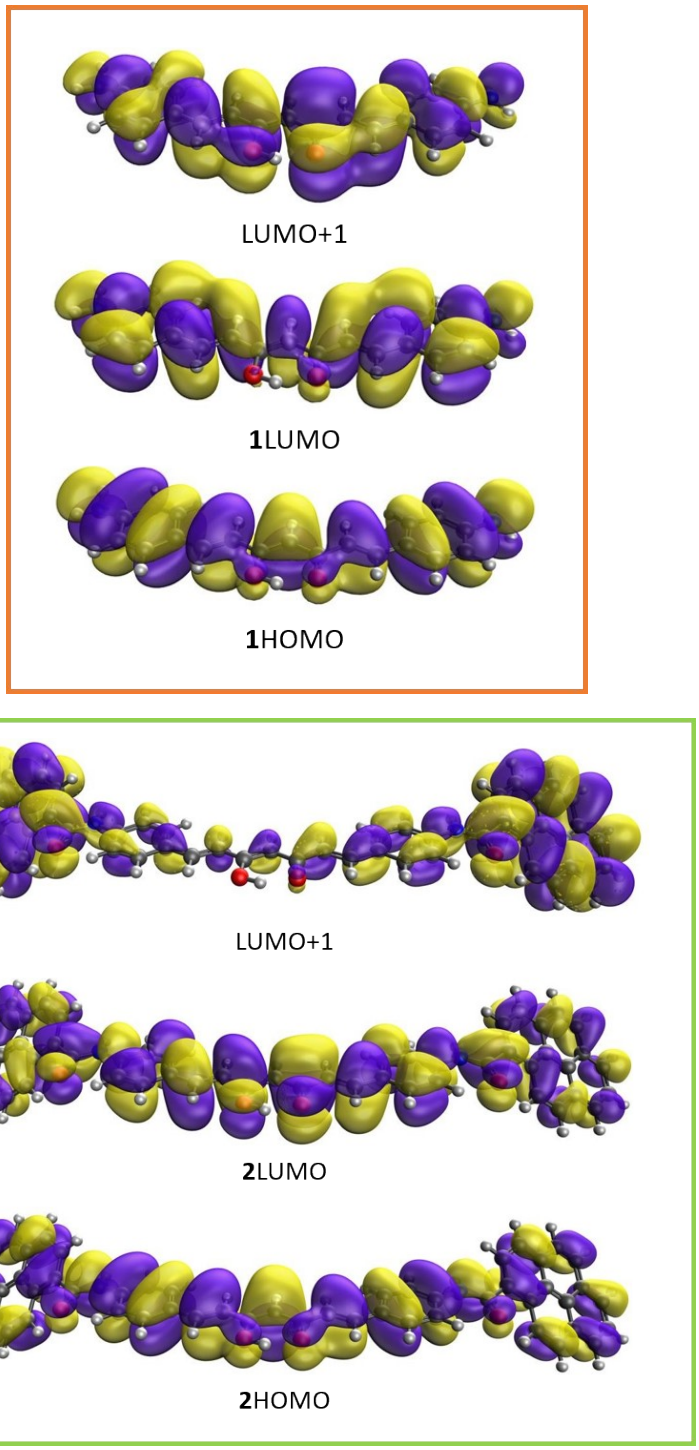

Figure S20. Frontier orbitals for the optimised structures of **1** (top, orange square) and **2** (bottom, green square) molecules using B3LYP calculations.

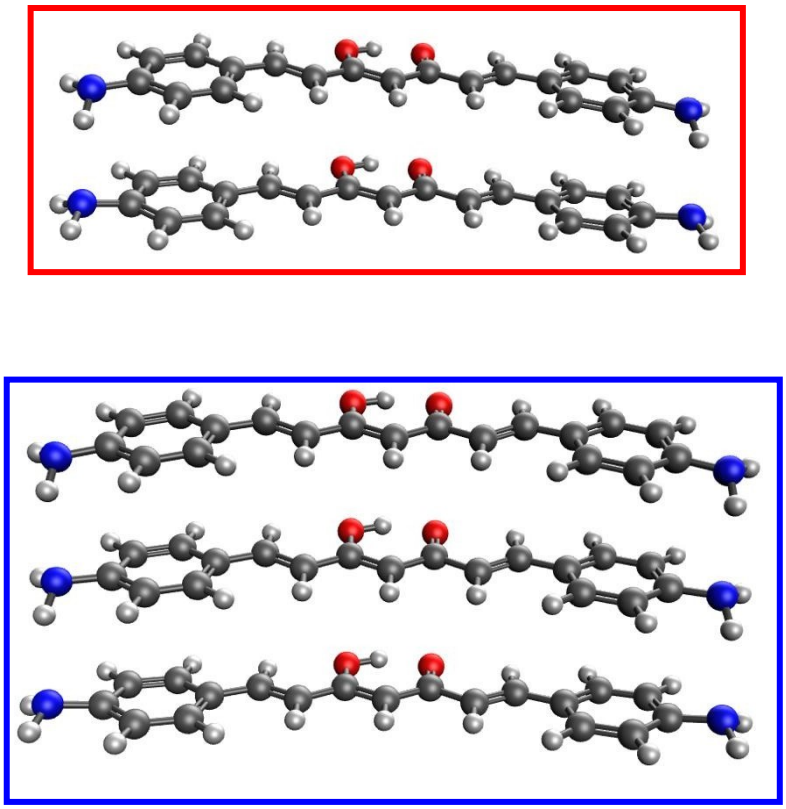

Figure S21. DFT optimised structure for the dimer (red box) and trimer (blue box) of **1**.

6. Molecular devices: fabrication and electrical measurements

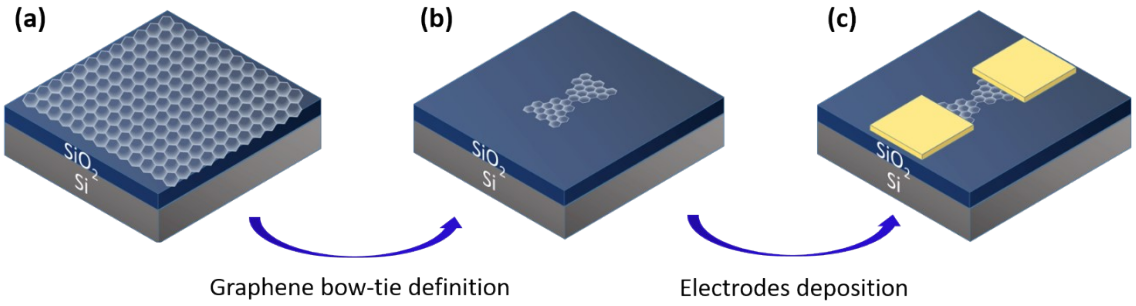

Figure S22. **Devices fabrication steps**. **(a)** 1 cm x 1 cm monolayer CVD graphene on 300 nm SiO_2 on doped silicon (used as back-gate) was purchased from Graphenea. **(b)** First, graphene is patterned into bow-tie shapes with a 400 nm wide constriction using e-beam lithography and oxygen plasma etching. **(c)** Contact pads are patterned using laser lithography followed by thermal evaporation of 5 nm chromium, as an adhesion layer, and 40 nm gold.

6.1 Electrical characterisation of GNJ.

We performed electroburning of 280 devices with initial resistance values between (2-20) KΩ. Of these, 154 (>55%) devices could be burnt while the remaining could not be opened after reaching a threshold resistance value, as already observed[11]. Most successfully burnt devices showed finite resistance values between (0.5-10) GΩ. In the other cases, the feedback control was not fast enough to prevent uncontrolled electroburning resulting in GNJs with infinite resistance values (>10 GΩ). The global statistics of the evolution of device resistances throughout the different stages of the experiment are depicted below.

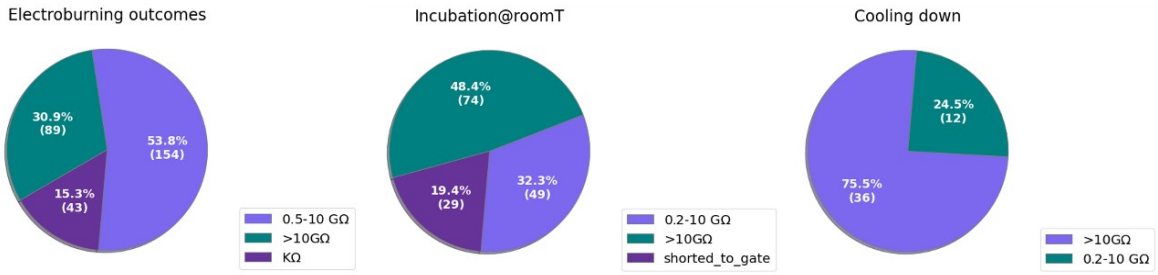

Figure S23. **Overview of experiment statistics**. Device distribution according to the values of zero bias resistances measured after each experiment step: electroburning, deposition of molecules at room temperature (Incubation@roomT) and cooling down.

After the cooling down, we report a redistribution of the device resistances towards values falling either in the very low or very high range, meaning gaps closing or opening to an infinite resistance (>10 GΩ). We attributed this occurrence to the building up of tensile stress in the graphene layer during the system's cooling down. Beyond this, the total number of measurable devices left after each experiment step decreases due to gate leakage.

Current-voltage characteristics of burnt devices with finite resistances were measured at room temperature and ambient pressure in the low bias voltage range (±200 mV). The set-up used to perform the electrical characterisation is custom-built at Delft University, and it consists of a low-noise IVVI-DAC rack together with a matrix module.

Devices showing tunneling-like I-Vs as that represented in Fig. S24 allow the estimation of the gap size by fitting the data through the Simmons model[12] assuming a rectangular potential barrier:

$$I = \frac{Ae}{h^2}\left[\left(\varphi - \frac{eV_{bias}}{2}\right) - e^{\left(-\frac{4\pi d}{h}\sqrt{2m\sqrt{\left(\varphi - \frac{eV_{bias}}{2}\right)}}\right)} + \left(\varphi + \frac{eV_{bias}}{2}\right) - e^{\left(-\frac{4\pi d}{h}\sqrt{2m\sqrt{\left(\varphi + \frac{eV}{2}\right)}}\right)}\right.$$

(Eq. S5)

where *e* and *m* are the elementary electron charge and mass, *h* is the Planck constant, φ the electrode's work function, which in the case of graphene is 4.3 eV. Finally, *A* is the area and *d* is the size of the nanogap. It is well known that when applying the Simmons model different parameter sets could lead to very similar curve families. A careful selection of the initial parameters is important when the uncertainty is higher, as in the case of the junction area. We can assume that *A* is greater than a single carbon atom and smaller than the initial bow-tie cross-section (400 nm) while for the height we can assume it to be equal to a single carbon atom. Considering this, we performed the Simmons fit using the two limiting area values corresponding to the above cases, i.e., 0.01 nm^2 and 100 nm^2. However, the difference between the resulting fitting parameters only affects higher decimals, and independently from the junction area, we obtain average values for the size of d = (2.4 ± 0.3) nm and φ = (1.7 ± 0.4) eV for the barrier height.

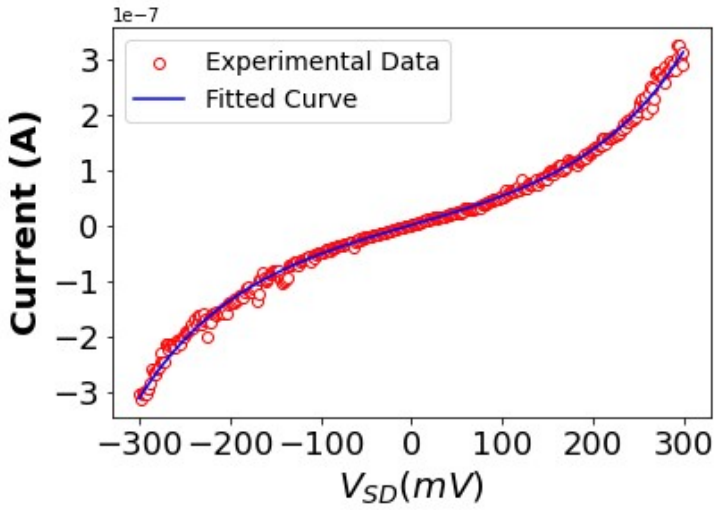

Figure S24. I-V bias characteristics of an open constriction. Current as a function of the voltage measured in an open constriction, showing an exponential dependence at bias voltages above hundreds of mV associated with single barrier tunnelling. The corresponding fit of the experimental data to the Simmons model is shown as the drawn blue line.

The I-V characteristics measured at different gate voltages are shown in Fig. S25 (a) with the corresponding differential conductance dI/dV represented as a function of the bias and gate

voltage (b), showing the absence of gate-voltage dependence. These observations are a strong indication that the GNJs are empty and applicable for the analysis of electron transport through single molecules.

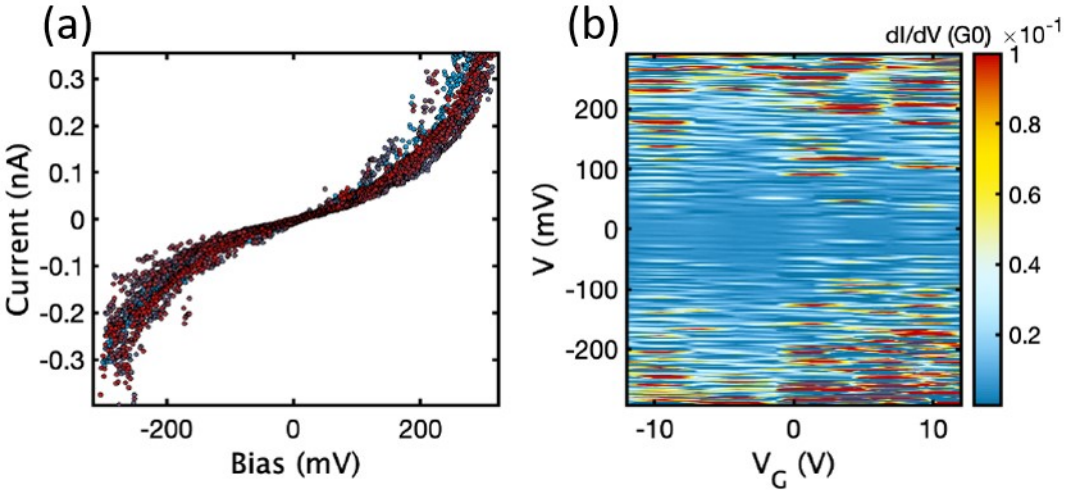

Figure S25. **Open junction characterization at room temperature**. **(a)** Current as a function of bias for different gate voltages of an open junction, and **(b)** corresponding differential conductance as a function of bias and gate voltage, compiled in a stability diagram highlighting the absence of gate dependence of I-V characteristics associated with current tunnelling.

6.2 Molecule deposition characterisation.

We have deposited pyACCMoid molecules on the graphene nano-junctions by dip coating of the devices for 1 hour in a 0.1 mM solution of the compound in THF. The pyrene groups are extended π systems that provide more robust stacking on graphene electrodes compared to anthracene groups alternatively used to functionalize graphene by π - π stacking interactions. The deposition method was selected after comparing the results of molecular functionalization of pristine graphene surfaces by drop casting and dip coating, as shown in the figure below.

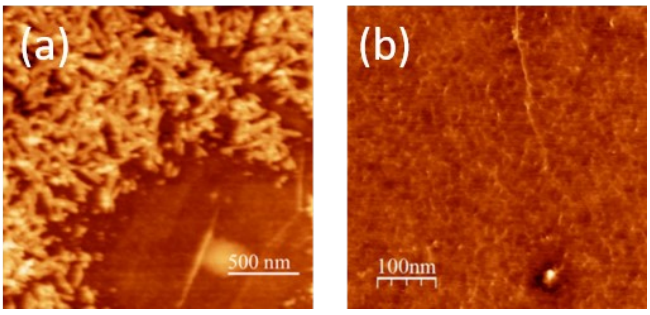

Figure S26. Molecular deposition. Atomic force microscope picture of the single-layer graphene substrate after drop cast of the pyACCMoid molecular solution in THF. Large polymerization on the surface is observed as a result of the drop cast of the compound **(a)**. When the molecules are deposited by dip coating the resulting repartition on the surface looks more uniform indicating less compound polymerization **(b)**.

6.3 Electrical characterisation of GNJs after molecule deposition at room temperature.

After the deposition of pyACCMoid molecules, we checked the zero-bias resistances of the junctions to select the ones with values between (0.2÷10) GΩ. Molecular resonances tend to occur far from the zero-gate window, and measurement of zero-bias conductance is, in general, not sufficient to detect changes after molecular functionalization. However, taking advantage of using a probe station, it is possible to move easily from device to device and perform a detailed check of the junction resistances beyond the initially selected. We measured resistances at zero gate voltage with values in the range (0.2÷10) GΩ for a total of 49 junctions. In the case of one junction, we detected changes in the gate dependence after molecular deposition at room temperature, Fig. S27.

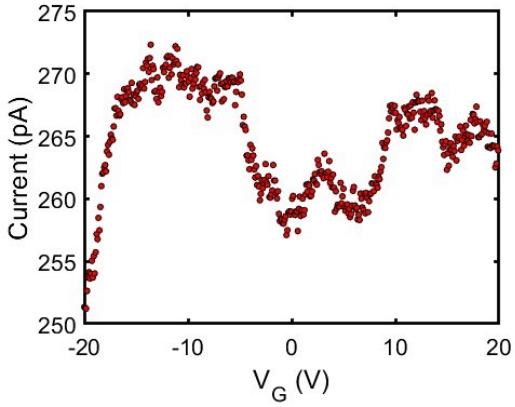

Figure S27. **Gate sweep at room temperature.** Current as a function of the gate voltage for fixed 10 mV bias (gate-sweep) measured at room temperature on a hybrid graphene-pyACCMoid NJ showing conductance variation of about 10 pA.

We characterized the device of Fig. S27 in more detail by measuring the current as a function of the bias and gate voltages compiled into the stability diagram that is shown in Fig. S28 (a) which displays a strong gate voltage dependence of the output current revealing a non-empty gap.

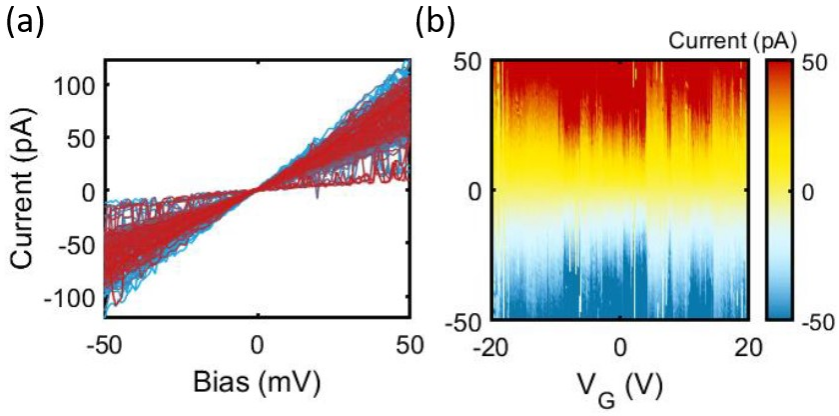

Figure S28. **Stability diagram at room temperature**. **(a)** Current as a function of bias voltage for different gate voltages measured after molecule deposition. **(b)** The stability diagram measured for the same device at room temperature shows gate modulation of the current (and thus conductance).

6.4 Electrical characterization of molecular junctions at low temperature.

Low-temperature measurements were carried out by using a cryogenic probe station (LakeShore) allowing reaching a temperature of about 10 K. After cooling down the system, we repeated the check of the zero-gate resistances across the junctions finding a total of 12 devices in the range of interest. Of these, we detected molecular resonances in 2 devices. Here, we report the results obtained from the current measurement as a function of the gate voltage for the other junction (*junction 2*) not described in the manuscript.

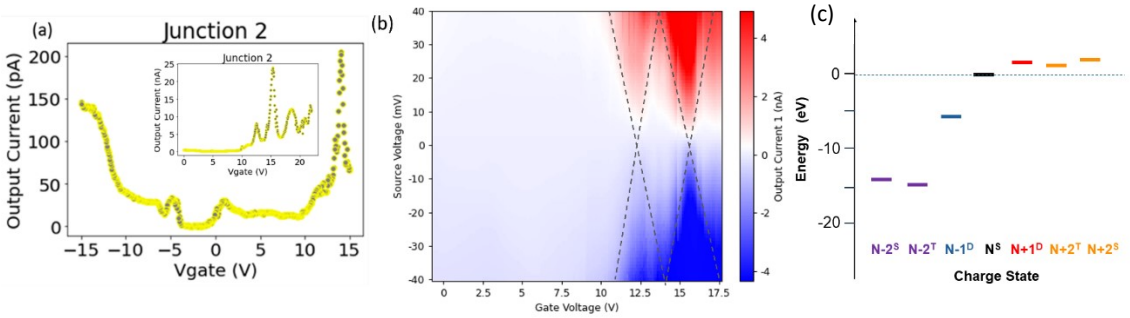

Figure S29. **Gate-sweeps and stability diagram of *junction 2* at low temperature**. Gate-sweep measured after molecule deposition and cool down to 10 K of a hybrid graphene molecular junction **(a)**. In the inset the same measurement taken in a following gate sweep in a reduced gate voltage range. **(b)** Stability diagram obtained in a subsequent measurement. Similar features with the stability diagram obtained for the other junction are found such as similar addition energy and gate couplings. Gate sweep shifting with the gate voltage is observed in the time interval between the two measurements' repetition. **(c)** Diagram with the calculated energies at the B3LYP level of the optimized structures keeping a planar structure for different oxidation states of **2** (S-singlet, D-doublet and T-triplet multiplicity).

Fig. S29 shows peak-like structures at V_G = 12.55 V; 15.20 V and 18.85 V and at V_G = -15 V and -5 V (inset of Fig.S29(a)). In both junctions, we observed a shift of the resonance peaks with the applied voltage during measurement repetitions, as illustrated in Fig. S30.

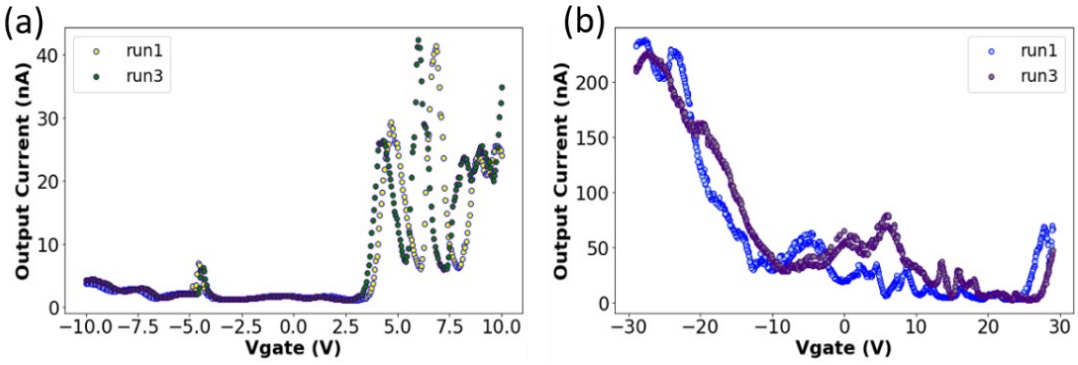

Figure S30. **Gate-sweep of a graphene hybrid molecular junction (a)** corresponds to the junction discussed in the main text, and **(b)** is the other pyACCMoid GNJ with gate-dependent features at low temperatures.

6.5 Electrostatic characterization.

Under the assumption of weak/intermediate molecular coupling to the electrodes, the transport process can be analysed by using the constant interaction model[13]. Accordingly, the gate coupling, α, is defined as[14]:

$$\alpha = \frac{1}{\frac{1}{\beta} + \frac{1}{\gamma}} \qquad (Eq.S6)$$

with β and γ being the positive, and negative, slopes of the Coulomb diamond (CD) edges, as represented in Fig. S35. In doing so, we find α =0.011 (1.1%) for the CD around V_G = -8 V (Fig. S31) and α = 0.005 (0.5%) for the diamond around V_G = -25 V (see Fig. 2(c) for the complete stability diagram).

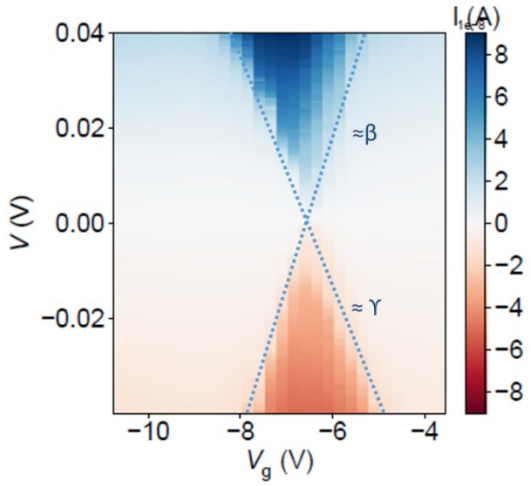

Figure S31. Stability diagram around a charge degeneracy point (CDP) for junction 1 at low temperature. The slopes separating the low- and high-current regions correspond to the relative source (C_S) and drain (C_D) capacitive couplings to the gate (C_G), labelled as $\gamma = C_G/C_S$ and $\beta = \frac{C_G}{C_S} + C_D$.

The existence of a non-negligible capacitive coupling between the contacting electrodes and the gate, as indicated by different values of gate couplings for distinct CDs, could result in resonances line in the SET regime running not parallel to the edges of the CD as highlighted by the dashed lines in Fig. S32 (a) below, displaying the numerical differential conductance $\frac{dI}{dV}$ as a function of bias and gate voltage for the CDP at V_G=-25 V (see Fig. 2(c)). Note that this CDP shifted in gate voltage by about -5 V between measurements displayed in Fig. 2(c) and the subsequent one depicted in Fig. S32 (a). The shift with the gate voltage is smaller for the CDP around -6 V as seen by the $\frac{dI}{dV}$ stability diagram shown in Fig. S32 (a). Both diamonds from Fig. S32 present features in the low-current regions with ON/OFF currents ratio of more than one order of magnitude (see Fig. S32 (a)) and shifting of the conduction resonances in the negative bias voltage with the gate voltage, as seen in the bottom right area of the same figure.

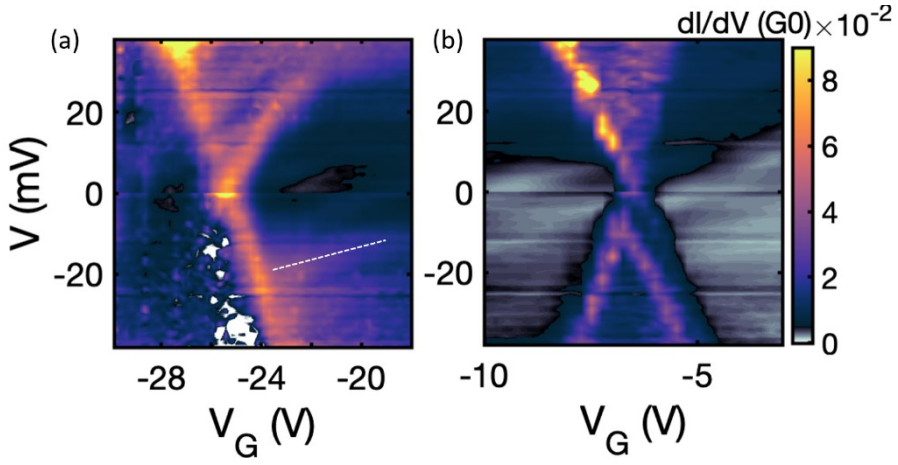

Figure S32 (a). Differential conductance, $\frac{dI}{dV}$ of high current regions in the negative gate voltage range around VG=-25 V and VG=-6 V **(b)**. Alternating high and low conduction resonances can be observed in the $\frac{dI}{dV}$ spectrum of (a) for the positive bias voltage range, as well as NDC for the negative bias voltages (white area). Here, it is also noted a missing edge of the diamond structure (bottom left area of the plot) and shifting of excitations with the gate voltage (bottom right area of the plot) with conduction lines running not parallel to the edge of the CD, as highlighted by the dotted line.

The large difference in gate coupling parameters ($\alpha(a) \approx 2\alpha(b)$ with *α(*a*)* and *α(*b*)* being the gate coupling calculated for the CDP's in Fig. 32 (a) and (b), respectively) is accompanied by opposite source-drain coupling asymmetry $: C_{D/S} = \frac{C_D}{C_S} = \frac{\beta}{\gamma} - \gamma$ giving $C_{D/S}(a) = 1.24$ and $C_{D/S}(b) = 0.69$. This suggests a different origin of the two CDPs. As discussed by Gehring *et al.*[15], the observation of conduction lines running not parallel to the edges of the diamond can be used to distinguish between molecular and electrode states, being the latter characterised by this feature. This is supported by the observation of negative differential conductance (NDC) for the CDP at V_G=-25 V in the negative bias voltage range as shown in the picture above.

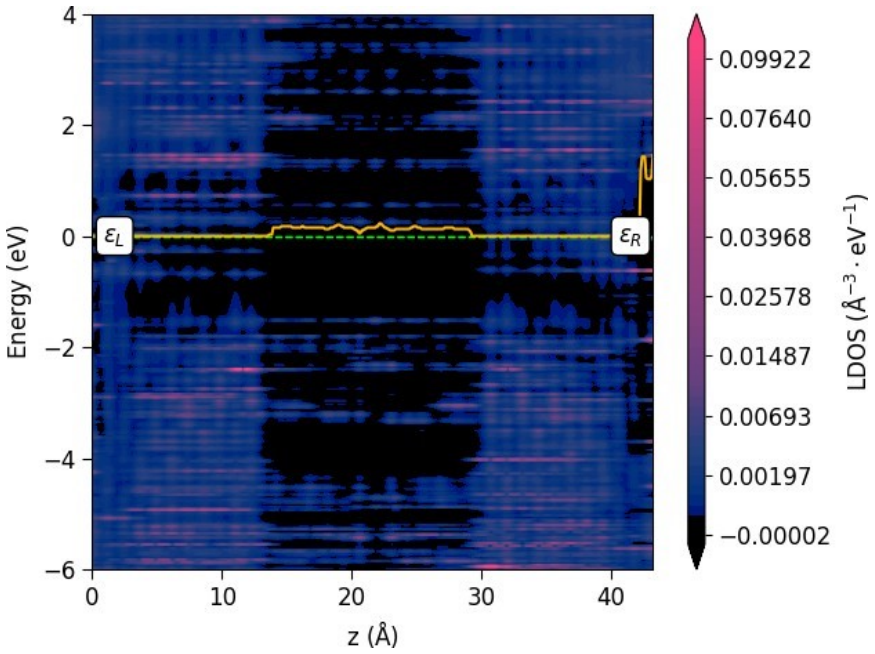

Theoretical calculations: part II.

Figure S33. Projected local density of states for molecule **2** on a graphene nano-gap. The x-axis corresponds to the distance of the left electrode in the device. Fermi level is highlighted in a dashed green line while the orange line indicates the energy of the conduction band edge.

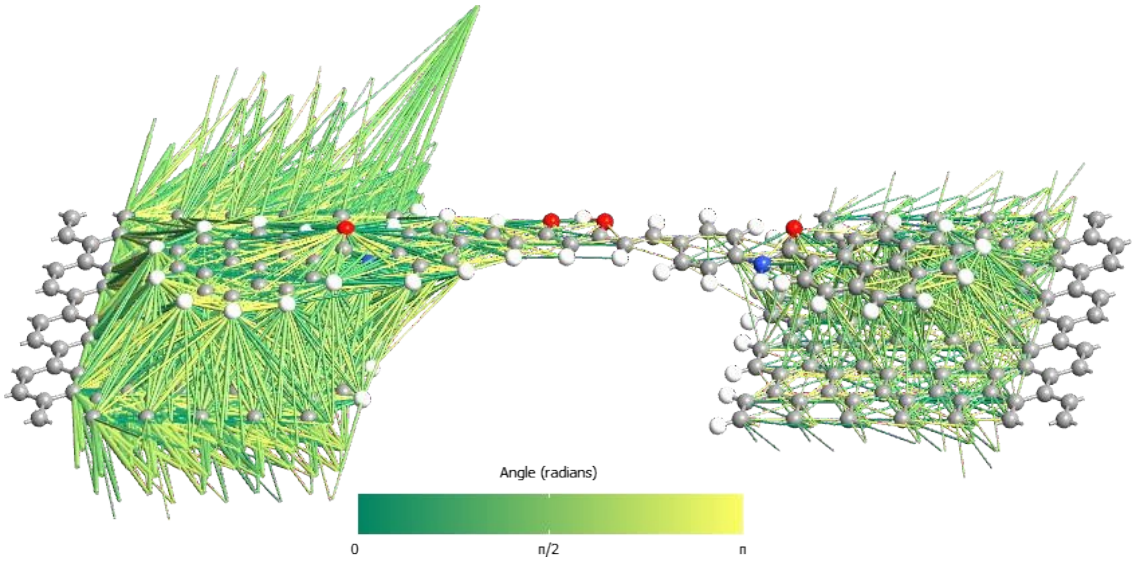

Figure S34. Transmission pathways for molecule **2** on a graphene nanogap. The colour of the arrows (in CCM) indicates the angle of the direction of the transport, green (0°, forward) and yellow (180°, backward), respectively, and intermediate colours (0–180°). The width of the arrow is proportional to the magnitude of the transport. A threshold value of 1×10^{-7} was

employed. Transmission pathways are calculated by the projection of the total transmission in pair contributions between atoms employing localised orbitals. This decomposition can be represented in real space by arrows indicating forward and backward current flow.

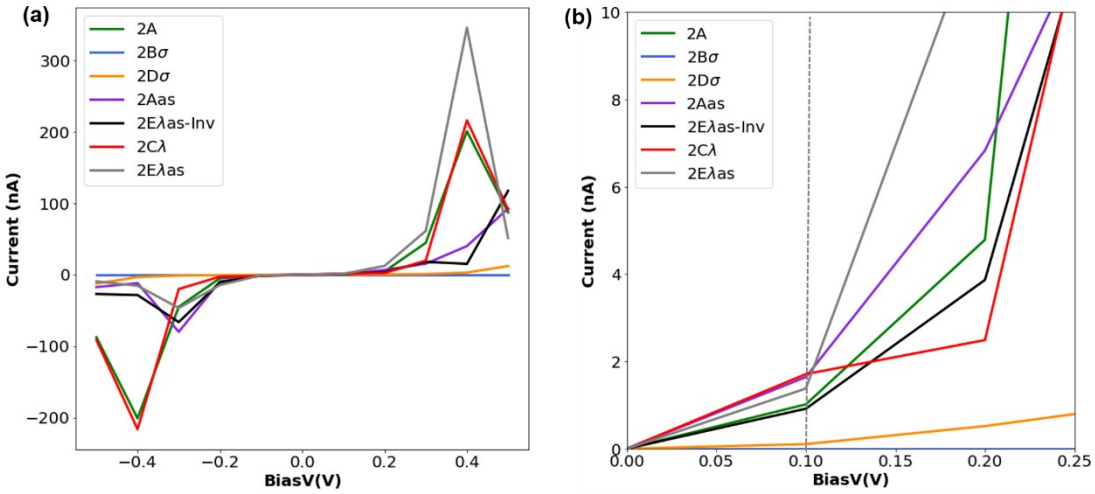

Figure S35. DFT calculated I-V characteristics for the configurations considered in Fig. 3 following the same colour code for the entire bias range applied in the experiments **(a)** and zoomed in the region up to 0.25 V **(b)**.

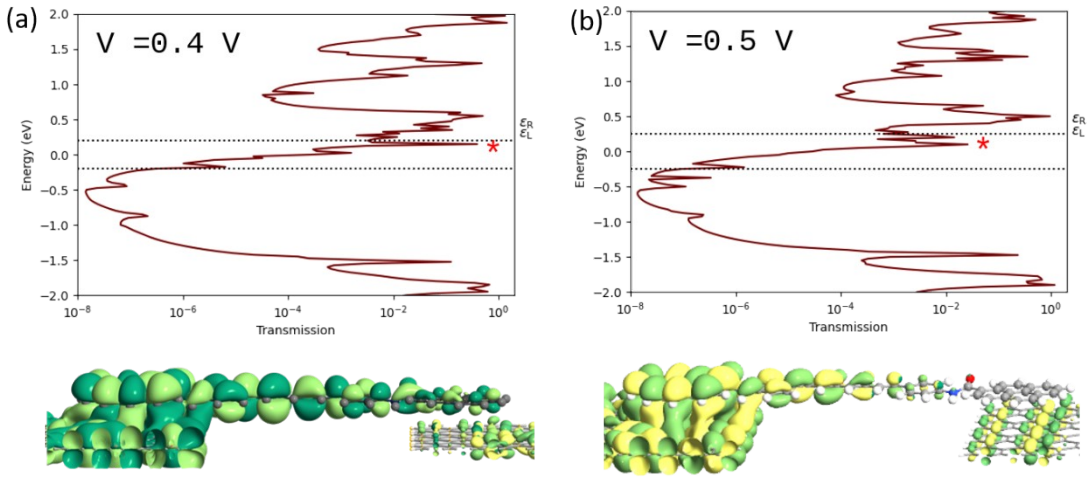

Figure S36. Transmission spectrum (in log scale) for the **2E$_{\lambda\text{-as}}$** configuration calculated for 0.4 V and 0.5 V to illustrate the NDC behaviour. Dotted lines indicate the limits of the bias window. The transmission eigenfunctions for the transmission peak are highlighted by the asterisk.

References

[1] Díaz-Torres, R. PhD Thesis, University of Barcelone (UB), 2018.

[2] Takahashi, T.; Hijikuro, I.; Sugimoto, H.; Kihara, T.; Shimmyo, Y.; Niidome, T. Preparation of Novel Curcumin Derivatives as Bsecretase Inhibitors. WO 2008066151 A1, 2008.

[3] Liu, J.; Huang, X.; Wang, F.; Hong, W. Quantum Interference Effects in Charge Transport through Single-Molecule Junctions: Detection, Manipulation, and Application. Acc. Chem. Res. 2019, 52 (1), 151–160. https://doi.org/10.1021/acs.accounts.8b00429.

[4] Liu, T.; Huang, Z.; Feng, R.; Ou, Z.; Wang, S.; Yang, L.; Ma, L. J. An Intermolecular Pyrene Excimer-Based Ratiometric Fluorescent Probes for Extremely Acidic PH and Its Applications. Dye. Pigment. 2020, 174 (November 2019), 108102. https://doi.org/10.1016/j.dyepig.2019.108102.

[5] Cuevas JC, Scheer E (2010) Molecular Electronics: An Introduction to Theory and Experiment World Scientific Series in Nanotechnology and Nanoscience. World Scientific Publishing Company, Singapore.

[6] Brandbyge, M.; Mozos, J. L.; Ordejon, P.; Taylor, J.; Stokbro, K., Density-functional method for nonequilibrium electron transport. *Physical Review B* 2002*,* 65, 165401.

[7] *Atomistix ToolKit ATK*, 2022.12; Synopsys, 2022.

[8] Perdew, J. P.; Burke, K.; Ernzerhof, M., Generalized gradient approximation made simple. *Phys. Rev. Lett.* 1996, 77, 3865-3868.

[9] Frisch, M. J.; Trucks, G. W.; Schlegel, H. B.; Scuseria, G. E.; Robb, M. A.; Cheeseman, J. R.; Scalmani, G.; Barone, V.; Mennucci, B.; Petersson, G. A.; Nakatsuji, H.; Caricato, M.; Li, X.; Hratchian, H. P.; Izmaylov, A. F.; Bloino, J.; Zheng, G.; Sonnenberg, J. L.; Hada, M.; Ehara, M.; Toyota, K.; Fukuda, R.; Hasegawa, J.; Ishida, M.; Nakajima, T.; Honda, Y.; Kitao, O.; Nakai, H.; Vreven, T.; Montgomery Jr., J. A.; Peralta, J. E.; Ogliaro, F.; Bearpark, M. J.; Heyd, J.; Brothers, E. N.; Kudin, K. N.; Staroverov, V. N.; Kobayashi, R.; Normand, J.; Raghavachari, K.; Rendell, A. P.; Burant, J. C.; Iyengar, S. S.; Tomasi, J.; Cossi, M.; Rega, N.; Millam, N. J.; Klene, M.; Knox, J. E.; Cross, J. B.; Bakken, V.; Adamo, C.; Jaramillo, J.; Gomperts, R.; Stratmann, R. E.; Yazyev, O.; Austin, A. J.; Cammi, R.; Pomelli, C.; Ochterski, J. W.; Martin, R. L.; Morokuma, K.; Zakrzewski, V. G.; Voth, G. A.; Salvador, P.; Dannenberg, J. J.; Dapprich, S.; Daniels, A. D.; Farkas, Ö.; Foresman, J. B.; Ortiz, J. V.; Cioslowski, J.; Fox, D. J.; Gaussian, Inc.: Wallingford, CT, USA, 2009.

[10] Becke, A.D. Density-functional thermochemistry .3. The role of the exact exchange. *J. Chem. Phys.* 1993, 98, 5648-5652.

[11] El Abbassi, M.; Pósa, L.; Makk, P.; Nef, C.; Thodkar, K.; Halbritter, A.; Calame, M. From Electroburning to Sublimation: Substrate and Environmental Effects in the Electrical Breakdown Process of Monolayer Graphene. Nanoscale 2017, 9 (44), 17312–17317. https://doi.org/10.1039/c7nr05348g.

[12] Simmons, J. G. Generalized Formula for the Electric Tunnel Effect between Similar Electrodes Separated by a Thin Insulating Film. J. Appl. Phys. 1963, 34

(6), 1793–1803. https://doi.org/10.1063/1.1702682.

[13] Limburg, B.; Thomas, J. O.; Sowa, J. K.; Willick, K.; Baugh, J.; Gauger, E. M.; Briggs, G. A. D.; Mol, J. A.; Anderson, H. L. Charge-State Assignment of Nanoscale Single-Electron Transistors from Their Current-Voltage Characteristics. Nanoscale 2019, 11 (31), 14820–14827. https://doi.org/10.1039/c9nr03754c.

[14] Thijssen, J. M.; Van Der Zant, H. S. J. Charge Transport and Single-Electron Effects in Nanoscale Systems. Phys. Status Solidi Basic Res. 2008, 245 (8), 1455–1470. https://doi.org/10.1002/pssb.200743470.

[15] Gehring, P.; Sowa, J. K.; Cremers, J.; Wu, Q.; Sadeghi, H.; Sheng, Y.; Warner, J. H.; Lambert, C. J.; Briggs, G. A. D.; Mol, J. A. Distinguishing Lead and Molecule States in Graphene-Based Single-Electron Transistors. ACS Nano 2017, 11 (6), 5325–5331. https://doi.org/10.1021/acsnano.7b00570.